Gradient-Based Predictive Pulse Pattern Control With Active Neutral Point Potential Balancing for Medium-Voltage Induction Motor Drives

Mirza Abdul Waris Begh, *Member, IEEE*, Petros Karamanakos, *Senior Member, IEEE*, and Tobias Geyer, *Fellow, IEEE*

***Abstract*—This paper presents a control method for medium-voltage (MV) drive systems consisting of a three-level neutral-point-clamped (NPC) inverter and an induction machine. The proposed approach aims to achieve stator current reference tracking and balancing of the neutral point (NP) potential in one computational stage, without the help of additional control loops. To this end, a model predictive control (MPC) algorithm, designed as a multiple-input multiple-output (MIMO) controller, manipulates optimized pulse patterns (OPPs) in real time. As a result, minimal current harmonic distortions are produced, while the NP potential is kept balanced both during steady-state and transient operating conditions. The effectiveness of the proposed control approach is validated in a real-time system by simulating the MV drive of interest in a hardware-in-the-loop (HIL) setting.**

***Index Terms*—Hardware-in-the-loop (HIL) simulations, model predictive control (MPC), medium-voltage (MV) drives, optimal control, optimized pulse patterns (OPPs), reference trajectory tracking.**

I. Introduction

MULTILEVEL converters are widely used to drive medium-voltage (MV) machines in industrial applications such as mining, smelting, traction, etc., due to their ability to efficiently handle high-power electrical energy conversion. To operate MV drives with high efficiency, operation at very low switching frequencies is required to minimize the switching power losses [1]. In practice, the switching frequency is typically limited between 200 Hz to 500 Hz, depending on the employed semiconductor devices, such as gate turn-off thyristors (GTOs) and gate commutated thyristors (GCTs) [2]. However, such low switching frequencies can lead to high current distortions, and thus adverse effects, such as increased losses in the machine. To address this issue, optimized pulse patterns (OPPs) can be employed as they produce the theoretical minimum current distortions [3], [4]. OPPs are switching sequences calculated offline, designed to have optimal harmonic properties [5]. The computation of the switch positions and switching angles of the OPPs involves solving a mathematical optimization problem that accounts for the total demand distortion (TDD) of the load current, e.g., the stator current of a machine [3], [4].

Control of OPPs, however, is a nontrivial task. This is due to the fact that OPPs do not have a fixed-length modulation interval, meaning that when sampling occurs, not only the fundamental component is sampled, but also the ripple. Moreover, the discontinuities in the switching angles with respect to the modulation index complicates the controller design. As a result, OPPs have been traditionally used with low-bandwidth controllers. Alas, such controllers cannot achieve satisfactory transient performance and disturbance rejection.

To address the above, high-bandwidth controllers that adopt the concept of trajectory tracking control have been proposed to manipulate OPPs in real time. For example, control methods based on deadbeat control principles were proposed in [5], [6], [7]. While the control scheme in [5] is based on the concept of stator *flux* trajectory tracking, the control scheme in [6], [7] utilizes the stator *current* trajectory. A more evolved controller designed in the framework of model predictive control (MPC)—known as model predictive pulse pattern control (MP^{3}C)—was presented in [8]. This method manipulates OPPs in real time and has been validated experimentally in industrial MV drive systems [9], [10]. In particular, MPC with OPPs is an attractive option since it can take advantage of the excellent steady-state performance and low current harmonic distortions attributed to OPPs as well as the fast dynamic responses that can be achieved with MPC. In this direction, the control method named gradient-based predictive pulse pattern control (GP^{3}C) was recently proposed [11] to achieve superior steady-state and dynamic performance for motor drive systems. The GP^{3}C method tracks the optimal stator current reference by *optimally* modifying the switching time instants of the nominal OPP.

Manuscript received 19 October 2023; revised 6 January 2024; accepted 14 March 2024. Date of publication 2 April 2024; date of current version 22 July 2024. Paper 2023-IPCC-1455.R1, presented at the 2022 IEEE Energy Conversion Congress and Exposition, Detroit, MI, USA, Dec. 01, and approved for publication in the IEEE Transactions on Industry Applications by the Industrial Power Converter Committee of the IEEE Industry Applications Society [DOI: 10.1109/ECCE50734.2022.9947782]. The work of Petros Karamanakos was supported by the Research Council of Finland. *(Corresponding author: Mirza Abdul Waris Begh.)*

Mirza Abdul Waris Begh and Petros Karamanakos are with the Faculty of Information Technology and Communication Sciences, Tampere University, 33101 Tampere, Finland (e-mail: mirza.begh@tuni.fi; p.karamanakos@ieee.org).

Tobias Geyer is with the ABB System Drives, 5300 Turgi, Switzerland (e-mail: t.geyer@ieee.org).

Color versions of one or more figures in this article are available at https://doi.org/10.1109/TIA.2024.3384353.

Digital Object Identifier 10.1109/TIA.2024.3384353

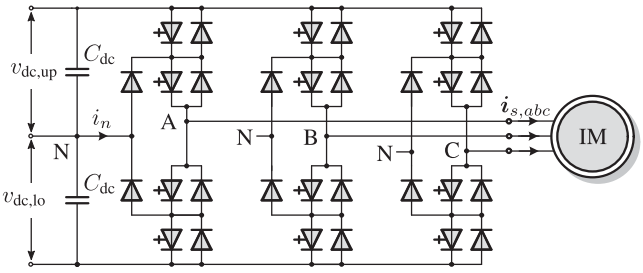

Fig. 1. Three-level neutral-point-clamped (NPC) voltage source inverter driving an induction machine.

TABLE I
RATED VALUES (LEFT) AND PARAMETERS (RIGHT) OF THE DRIVE

Induction motor	Voltage	3300 V	R_s	0.0108 p.u.
	Current	356 A	R_r	0.0091 p.u.
	Real power	1.646 MW	X_{ls}	0.1493 p.u.
	Apparent power	2.034 MVA	X_{lr}	0.1104 p.u.
	Stator frequency	$2\pi 50$ rad/s	X_m	2.3489 p.u.
	Rotational speed	596 rpm		
	Torque	26.2 kNm		
	Inertia	50 kgm^2		
Inverter	Dc-link voltage	5200 V	V_{dc}	1.9299 p.u.
	Dc-link capacitance	2.24 mF	X_{dc}	3.7628 p.u.

Nevertheless, the above-mentioned control techniques must fulfill additional control objectives when multilevel converters are considered as their internal voltages need to be balanced during the whole operation of the system. For example, when neutral-point-clamped (NPC) inverters are of interest, the neutral point (NP) potential should be kept around zero to avoid deviations of the phase voltages from the expected voltage levels. Hence, even though the NPC inverter has an inherent natural balancing mechanism [12], active balancing techniques are commonly employed to prevent the NP potential from drifting away.

To this aim, a variety of control strategies have been used to tackle the problem of NP potential balancing. Most of these methods are based on the manipulation of the common-mode component of the output voltage [13], [14], [15]. Therefore, control of the NP potential is achieved by using an outer loop to manipulate the common-mode component of the reference voltage that is fed to the modulator. Alternatively, control of the NP potential can be achieved by exploiting the redundant switching vectors of the NPC inverter [16]. It should be noted, however, that the effectiveness of these methods diminishes as the phase difference between the inverter voltage and current approaches 90° [15].

Addition of external loops, however, can further limit the controller bandwidth. For this reason, the developed closed-loop control methods that manipulate OPPs aim at incorporating the NP potential balancing mechanism into the inner control loop. In this direction, similar to [16], [17] adopts the concept of redundant vector manipulation. By selecting appropriate redundant sub-bridges during steady-state and transient operation, the control method eliminates the NP potential error at low modulation indices while operating the power converter at low switching frequencies. In [18], a push-pull configuration for a variable-speed drive is presented where a five-level OPP is mapped into two three-level OPPs for two NPC inverters. This gives rise to an additional degree of freedom which can be utilized to balance the NP potential. In [19], the MP^{3}C method addresses the balancing of the NP potential by adding an extra term to the objective function to penalize the deviation of the dc component of the NP potential from its reference. Nevertheless, during the derivation of the control problem, a number of assumptions are made that can compromise the overall performance of the control scheme. As a result, the controller design becomes more complicated.

Motivated by the above, this paper refines the GP^{3}C method [11] to tackle the problem of the NP potential balancing in a simple, yet effective, manner.[1] By exploiting the high design versatility of GP^{3}C attributed to its modeling principle, i.e., the use of the gradient of the system output to predict its evolution, the current control and NP potential balancing problems are tackled in one computational stage. In doing so, unlike traditional balancing methods, the proposed method does not rely on manipulating the common-mode voltage of the inverter, but it rather directly regulates the (instantaneous) NP potential along its reference.[2] This equips the GP^{3}C method with a high bandwidth and a high degree of disturbance rejection. The efficacy of the proposed method is verified using real-time tests performed in a hardware-in-the-loop (HIL) environment based on a variable speed MV drive system.

The remainder of this paper is organized as follows. Section II presents the model of the MV VSD system adopted for the case study. Following, the proposed GP^{3}C algorithm is presented in Section III along with the formulation of the optimal control problem as a quadratic program (QP). Section IV assesses the performance of the proposed control strategy during steady-state and transient operating conditions based on real-time HIL simulations. Finally, Section V concludes this article.

II. MODEL OF THE MV DRIVE SYSTEM

Consider the MV variable speed drive system in Fig. 1 consisting of a three-level NPC voltage source inverter and an induction machine (IM) with the rated values and parameters provided in Table I. The mathematical model of the system is derived in the stationary $\alpha\beta$-frame, where the transformation matrix

$$\boldsymbol{K} = \frac{2}{3}\begin{bmatrix} 1 & -\frac{1}{2} & -\frac{1}{2} \\ 0 & \frac{\sqrt{3}}{2} & -\frac{\sqrt{3}}{2} \end{bmatrix}, \tag{1}$$

is used to transform the three-phase quantities into the $\alpha\beta$-frame. Throughout this paper, the quantities are normalized and presented in the per unit (p.u.) system.

The dc link of the inverter comprises two identical capacitors C_{dc} with (inverse) reactance X_{dc}; the midpoint N is the so-called

[1] This paper is an extension of [20]. Herein, the performance of the proposed method is verified under several operating conditions using real-time tests performed in a hardware-in-the-loop (HIL) environment.

[2] It should be noted that the proposed control method does not aim to reduce the ripple of the NP potential during steady-state operation, as this is a natural characteristic of the NP potential v_n.

NP. The total (constant) dc-link voltage is

$$V_{\text{dc}} = v_{\text{dc,up}} + v_{\text{dc,lo}}, \tag{2}$$

where $v_{\text{dc,up}}$ and $v_{\text{dc,lo}}$ denote the upper and the lower dc-link capacitor voltages, respectively. Depending on the *single-phase* switch position $u_x \in \{-1, 0, 1\}$ in phase $x \in \{a, b, c\}$ the inverter can produce three possible phase voltage levels, namely $v_{\text{dc,lo}}$, 0, and $v_{\text{dc,up}}$, respectively. Hence, the three-phase output voltage of the inverter in the $\alpha\beta$-frame is a function of the *three-phase* switch position $\boldsymbol{u}_{abc} = [u_a \;\; u_b \;\; u_c]^T$, and it is given by

$$\boldsymbol{v}_s = \frac{v_{\text{dc}}}{2}\boldsymbol{K}\boldsymbol{u}_{abc} - v_n\boldsymbol{K}\left|\boldsymbol{u}_{abc}\right|, \tag{3}$$

where $|\boldsymbol{u}_{abc}| = [|u_a| \;\; |u_b| \;\; |u_c|]^T$ is the component-wise absolute value of the three-phase switch position. Note that since the inverter is driving a machine, the output voltage of the inverter is equal to the stator voltage $\boldsymbol{v}_s$.

As can be seen in (3), the output inverter voltage fluctuates with the NP potential, defined as

$$v_n = \frac{1}{2}(v_{\text{dc,lo}} - v_{\text{dc,up}}). \tag{4}$$

This potential evolves as a function of the current flowing through the NP [21], i.e.,

$$\frac{\mathrm{d}v_n}{\mathrm{d}t} = \frac{1}{2}\left(\frac{\mathrm{d}v_{\text{dc,lo}}}{\mathrm{d}t} - \frac{\mathrm{d}v_{\text{dc,up}}}{\mathrm{d}t}\right) = -\frac{1}{2X_{\text{dc}}}i_n. \tag{5}$$

The NP current i_n changes when a phase current i_{sx} flows through the NP. This happens when the corresponding switch position u_x is zero, meaning that i_n is a function of $\boldsymbol{u}_{abc}$ and the inverter (i.e., stator) current $\boldsymbol{i}_{s,abc} = [i_{sa} \;\; i_{sb} \;\; i_{sc}]^T$ according to

$$\begin{aligned} i_n &= (1 - |u_a|)i_{sa} + (1 - |u_b|)i_{sb} \\ &\quad + (1 - |u_c|)i_{sc} = -\left|\boldsymbol{u}_{abc}\right|^T \boldsymbol{i}_{abc}, \end{aligned} \tag{6}$$

where a star connection for the load is assumed, i.e., $i_{sa} + i_{sb} + i_{sc} = 0$. Using (5) and (6), the evolution of the NP potential can be written as

$$\frac{\mathrm{d}v_n}{\mathrm{d}t} = \frac{1}{2X_{\text{dc}}}\left|\boldsymbol{u}_{abc}\right|^T \boldsymbol{i}_{abc}. \tag{7}$$

Regarding the dynamics of the squirrel cage IM in Fig. 1, these can be described by the differential equations of the stator current $\boldsymbol{i}_s$ and the rotor flux $\boldsymbol{\psi}_r$,[3] i.e., [22]

$$\frac{\mathrm{d}\boldsymbol{i}_s}{\mathrm{d}t} = -\frac{1}{\tau_s}\boldsymbol{i}_s + \left(\frac{1}{\tau_r}\boldsymbol{I}_2 - \omega_{\text{r}}\begin{bmatrix}0 & -1\\ 1 & 0\end{bmatrix}\right)\frac{X_m}{D}\boldsymbol{\psi}_r + \frac{X_r}{D}\boldsymbol{v}_s, \tag{8a}$$

$$\frac{\mathrm{d}\boldsymbol{\psi}_r}{\mathrm{d}t} = \frac{X_m}{\tau_r}\boldsymbol{i}_s - \frac{1}{\tau_r}\boldsymbol{\psi}_r + \omega_{\text{r}}\begin{bmatrix}0 & -1\\ 1 & 0\end{bmatrix}\boldsymbol{\psi}_r. \tag{8b}$$

In (8), R_s and R_r are the stator and rotor resistance, respectively, while X_{ls}, X_{lr}, and X_m are the stator leakage, rotor leakage, and mutual reactance, respectively. Moreover, $\tau_s = X_r D/(R_s X_r^2 + R_r X_m^2)$ and $\tau_r = X_r/R_r$, are the transient stator and rotor time constants, respectively, while the constant D is defined as $D = X_s X_r - X_m^2$, with $X_s = X_{ls} + X_m$ and $X_r = X_{lr} + X_m$. In addition, ω_r is the angular rotor speed. Finally, $\boldsymbol{I}_2$ is the two-dimensional identity matrix.

[3]Note that the mechanical dynamics are neglected in the subsequent modeling—and the prediction model—as they are slower than the electrical dynamics.

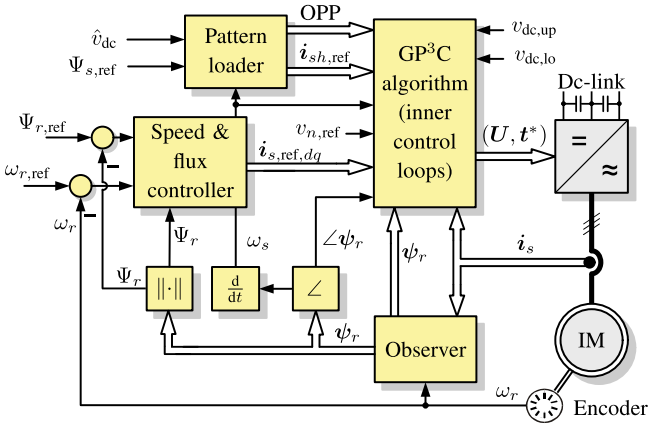

Fig. 2. Block diagram of the outer control loops of the GP³C scheme.

Let us consider the three-phase switch position $\boldsymbol{u}_{abc}$ as input to the drive system, the stator current and NP potential as the system output, i.e., $\boldsymbol{y} = [i_{s\alpha} \;\; i_{s\beta} \;\; v_n]^T \in \mathbb{R}^3$, and the stator current, rotor flux and the NP potential as the system state, i.e., the state vector is $\boldsymbol{x} = [i_{s\alpha} \;\; i_{s\beta} \;\; \psi_{r\alpha} \;\; \psi_{r\beta} \;\; v_n]^T \in \mathbb{R}^5$. By using (7) and (8), the continuous-time state-space model of the drive system is written as

$$\frac{\mathrm{d}\boldsymbol{x}(t)}{\mathrm{d}t} = \boldsymbol{F}(t)\boldsymbol{x}(t) + \boldsymbol{G}\boldsymbol{u}_{abc}(t) \tag{9a}$$

$$\boldsymbol{y}(t) = \boldsymbol{C}\boldsymbol{x}(t), \tag{9b}$$

where the system $\boldsymbol{F}(t) \in \mathbb{R}^{5\times5}$, input $\boldsymbol{G} \in \mathbb{R}^{5\times3}$, and output $\boldsymbol{C} \in \mathbb{R}^{3\times5}$ matrices are provided in Appendix A. It is important to point out that the system matrix $\boldsymbol{F}(t)$ contains nonlinear terms due to the nonlinear NP dynamics. Such a characteristic poses difficulties from a controller design perspective.

Subsequently, (9) is discretized with the sampling interval T_s by employing forward Euler discretization. In doing so, the discrete-time state-space model of the drive is computed as

$$\boldsymbol{x}(k+1) = \boldsymbol{A}(k)\boldsymbol{x}(k) + \boldsymbol{B}\boldsymbol{u}_{abc}(k) \tag{10a}$$

$$\boldsymbol{y}(k) = \boldsymbol{C}\boldsymbol{x}(k), \tag{10b}$$

where $\boldsymbol{A}(k) = \boldsymbol{I}_5 + \boldsymbol{F}(t)T_s$ and $\boldsymbol{B} = \boldsymbol{G}T_s$ are the discrete-time matrices, and $k \in \mathbb{N}$ denotes the discrete time step.

III. GP³C with Active NP Potential Balancing

The proposed GP³C control scheme exploits the inherent characteristics of OPPs [3], [4] and gradient-based direct MPC [23], [24], [25]. In the sequel, the control problem and the working principles of the algorithm are presented. The block diagram of the presented control algorithm is given in Fig. 2.

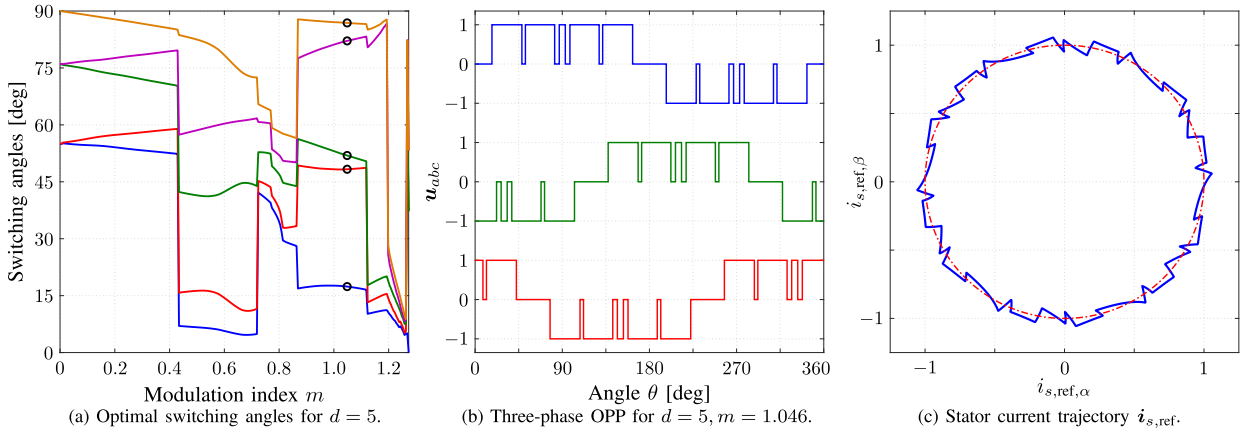

(a) Optimal switching angles for $d = 5$. (b) Three-phase OPP for $d = 5, m = 1.046$. (c) Stator current trajectory $\boldsymbol{i}_{s,\mathrm{ref}}$.

Fig. 3. (a) OPP $\boldsymbol{p}(d, m)$ for a three-level converter with $d = 5$ switching angles per quarter of the fundamental period. The optimal switching angles for the modulation index $m = 1.046$ are indicated by (black) circles. (b) Three-phase OPP for $m = 1.046$. (c) The current reference trajectory (solid blue line) for the given three-phase OPP is a combination of the fundamental component $\boldsymbol{i}_{s1,\mathrm{ref}}$ (red dash-dotted line) and the harmonic component $\boldsymbol{i}_{sh,\mathrm{ref}}$.

A. Preliminaries

OPPs are computed in an offline procedure by solving an optimization problem that typically accounts for the TDD of the stator current. This problem is solved for a given pulse number d and yields a set of optimal switching angles as a function of the modulation index m. Fig. 3(a) shows the optimal switching angles for the OPP $\boldsymbol{p}(d, m)$, with $d = 5$, over the whole range of modulation indices $m \in [0, 4/\pi]$. For a given set of switching angles, the three-phase OPP can be constructed at a given modulation index, by assuming quarter- and half-wave symmetry as well as a balanced three-phase system. As an example, the three-phase OPP $\boldsymbol{p}(5, 1.046)$ is depicted in Fig. 3(b). Furthermore, based on a given OPP, the steady-state current trajectory (Fig. 3(c)) can be computed, as explained in [11].

B. Control Problem

Consider a prediction horizon T_p of finite length, i.e., $T_p = N_p T_s$, where $N_p \in \mathbb{N}^+$ is the number of prediction steps. Let $z \in \mathbb{N}$ be the number of switching time instants of the nominal OPP that fall within the horizon T_p. Moreover, for controller design purposes, the following vectors are introduced

$$\boldsymbol{t}_{\mathrm{ref}} = \begin{bmatrix} t_{1,\mathrm{ref}} & t_{2,\mathrm{ref}} & \dots & t_{z,\mathrm{ref}} \end{bmatrix}^T, \tag{11a}$$

$$\boldsymbol{U} = \begin{bmatrix} \boldsymbol{u}_{abc}^T(t_0) & \boldsymbol{u}_{abc}^T(t_{1,\mathrm{ref}}) & \dots & \boldsymbol{u}_{abc}^T(t_{z,\mathrm{ref}}) \end{bmatrix}^T, \tag{11b}$$

$$\boldsymbol{t} = \begin{bmatrix} t_1 & t_2 & \dots & t_z \end{bmatrix}^T, \tag{11c}$$

where $\boldsymbol{t}_{\mathrm{ref}} \in \mathbb{R}^z$ is the vector of switching time instants of the nominal OPP that fall within T_p, $\boldsymbol{U} \in \mathcal{U}^{3(z+1)}$ is the vector of the corresponding OPP switch positions,[4] and $\boldsymbol{t} \in \mathbb{R}^z$ includes the to-be-computed modified switching time instants.

The discussed control algorithm aims to regulate the stator current $\boldsymbol{i}_s$ along its optimal reference trajectory $\boldsymbol{i}_{s,\mathrm{ref}}$ by manipulating (i.e., modifying) the switching time instants of the nominal OPP $\boldsymbol{t}_{\mathrm{ref}}$ such that minimal current distortions are achieved in steady state. Moreover, the voltage over the upper and lower dc-link capacitors, $v_{\mathrm{dc,up}}$ and $v_{\mathrm{dc,lo}}$, respectively, should be balanced by minimizing the deviation of the NP potential v_n from its reference $v_{n,\mathrm{ref}}$. These goals are to be achieved while modifying the nominal OPP as little as possible. Finally during transients, the controller should exhibit high bandwidth to achieve fast dynamic performance.

To meet the above-mentioned objectives, the control scheme is formulated as a constrained optimization problem. Specifically, the objective function that captures the output tracking error and the changes in the switching time instants is[5]

$$J = \sum_{i=1}^{z} \left\| \boldsymbol{y}_{\mathrm{ref}}(t_{i,\mathrm{ref}}) - \boldsymbol{y}(t_i) \right\|_{\boldsymbol{Q}}^2 + \lambda_t \left\| \Delta \boldsymbol{t} \right\|_2^2 , \tag{12}$$

with $\boldsymbol{y}_{\mathrm{ref}}$ being the output reference vector, i.e., $\boldsymbol{y}_{\mathrm{ref}} = [\boldsymbol{i}_{s,\mathrm{ref}}^T \;\; v_{n,\mathrm{ref}}]^T \in \mathbb{R}^3$, and $\boldsymbol{Q} = \mathrm{diag}(1 \;\; 1 \;\; \lambda_n) \in \mathbb{R}^{3\times 3}$ being a diagonal positive-definite matrix, whose entries penalize the deviation of the output variables from their respective references, i.e., $\boldsymbol{i}_s - \boldsymbol{i}_{s,\mathrm{ref}}$ and $v_n - v_{n,\mathrm{ref}}$.[6] Moreover, $\Delta \boldsymbol{t} = \boldsymbol{t}_{\mathrm{ref}} - \boldsymbol{t}$ denotes the (*to-be-applied*) modifications on the nominal OPP. The weighting factor $\lambda_t \geq 0$ penalizes the deviation of the modified switching time instants with respect to the nominal OPP, and thus serves as a tuning parameter to prioritize between the output tracking and allowed modifications in the nominal OPP.

Function (12) needs to be minimized to obtain the vector of modified switching time instants $\boldsymbol{t}$. To do so, the evolution of the output variables within the prediction horizon must be computed. As the OPP switch positions $\boldsymbol{u}_{abc}$ that fall within T_p are known, see the switching sequences $\boldsymbol{U}$ (11b), the evolution of the system output can be computed based on its gradient.

[4]The first entry in $\boldsymbol{U}$ represents the switch position at the end of the last sampling interval, i.e., $\boldsymbol{u}_{abc}(t_0^-)$.

[5]The expression $\|\boldsymbol{\xi}\|_{\boldsymbol{Q}}^2$ denotes the squared norm of a vector $\boldsymbol{\xi}$ weighted with the matrix $\boldsymbol{Q}$.

[6]The reference of the NP potential $v_{n,\mathrm{ref}}$ is zero.

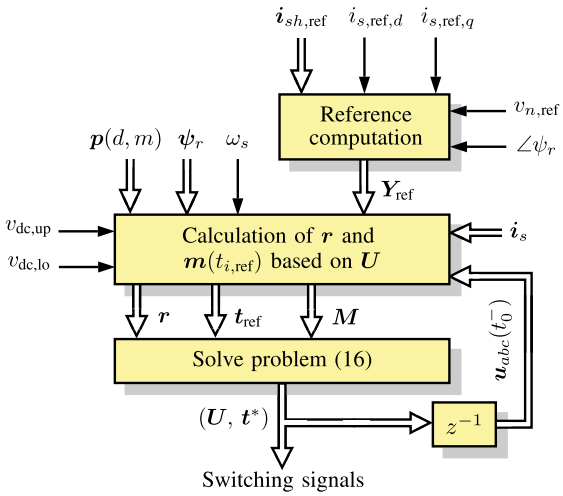

Fig. 4. Inner control loops of the GP^{3}C algorithm.

Algorithm 1: GP^{3}C With Active NP Potential Balancing.

Given $\boldsymbol{u}_{abc}(t_0)$, $\boldsymbol{x}(t_0)$, $\boldsymbol{i}_{s,\mathrm{ref},dq}$, $v_{n,\mathrm{ref}}$ and $\boldsymbol{p}(d,m)$

0. Extract the z switching time instants and switch positions that fall within T_p from the nominal OPP $\boldsymbol{p}(d,m)$ to formulate $\boldsymbol{t}_{\mathrm{ref}}$ and $\boldsymbol{U}$.
1. Compute the reference values of outputs $\boldsymbol{y}_{\mathrm{ref}}(t_{i,\mathrm{ref}})$, $i \in \{1,2,\ldots,z\}$.
2. Formulate the gradients $\boldsymbol{m}(t_{\ell,\mathrm{ref}})$, $\ell \in \{0,1,2,\ldots,z-1\}$.
3. Solve the optimization problem (16). This yields $\boldsymbol{t}^*$.

Return $\boldsymbol{t}^*(k)$ that fall within T_s and modify the OPP accordingly.

Specifically, it can be assumed that the output evolves with a constant gradient within each subinterval $\Delta t_{\ell,\mathrm{ref}}$, where

$$\Delta t_{\ell,\mathrm{ref}} = t_{\ell+1,\mathrm{ref}} - t_{\ell,\mathrm{ref}}\,, \tag{13}$$

with $\ell \in \{0,1,2,\ldots,z-1\}$, and $t_{0,\mathrm{ref}} \equiv t_0 \equiv kT_s$. As a result, the output trajectories can be described by their associated gradients, i.e.,

$$\boldsymbol{m}(t_{\ell,\mathrm{ref}}) = \frac{\boldsymbol{y}(t_{\ell+1,\mathrm{ref}}) - \boldsymbol{y}(t_{\ell,\mathrm{ref}})}{\Delta t_{\ell,\mathrm{ref}}} = \boldsymbol{C}\frac{\boldsymbol{x}(t_{\ell+1,\mathrm{ref}}) - \boldsymbol{x}(t_{\ell,\mathrm{ref}})}{\Delta t_{\ell,\mathrm{ref}}}\,. \tag{14}$$

Note that in (14), the gradients at the nominal OPP switching instants $t_{1,\mathrm{ref}}, t_{2,\mathrm{ref}}, \ldots, t_{z,\mathrm{ref}}$ are dependent on the predicted state, i.e., $\boldsymbol{x}(t_{1,\mathrm{ref}})$, $\boldsymbol{x}(t_{2,\mathrm{ref}})$, $\ldots$, $\boldsymbol{x}(t_{z,\mathrm{ref}})$, respectively, to provide the most accurate computation of the corresponding gradient. This is accomplished by employing the discrete-time system model (10).

Finally, based on the above expressions and by introducing some assumptions as outlined in [11], the objective function (12) is rewritten as

$$J = \|\boldsymbol{r} - \boldsymbol{M}\boldsymbol{t}\|_{\boldsymbol{Q}}^2 + \lambda_t \|\Delta \boldsymbol{t}\|_2^2\,, \tag{15}$$

where $\boldsymbol{r}$ is a vector that depends on the reference values and measurements of the outputs, and $\boldsymbol{M}$ is a matrix of the slopes with which the controlled variables evolve over the prediction horizon, see Appendix B.

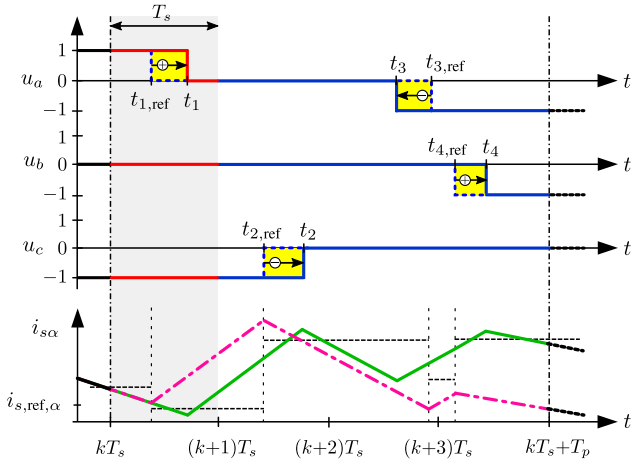

Fig. 5. Example of trajectory tracking of GP^{3}C for one of the controlled variables (e.g., stator current $i_{s\alpha}$) within a four-step ($T_p = 4T_s$) prediction horizon. The nominal OPP instants $t_{i,\mathrm{ref}}$ (dotted line) and the modified switching instants t_i (solid line) are shown, where $i \in \{1,2,3,4\}$. The modifications introduced by the controller are highlighted in yellow. In the bottom figure, the dash-dotted (magenta) line represents the current trajectory when applying the nominal OPP, while the solid (green) line shows the current trajectory based on the modified pulse pattern. The dashed (black) line is the current reference sampled at the nominal OPP time instants.

C. Control Algorithm

The proposed control method is designed in the discrete-time domain and works at equally spaced time instants kT_s. The block diagram of the inner control loop is shown in Fig. 4. Furthermore, Algorithm 1 provides the pseudocode of the proposed control method.

Before the control algorithm is executed, the offline computed nominal OPP and harmonic current references are retrieved from the look-up tables (LUTs) where they are stored. With this, the three-phase OPP is computed and the stator current reference over the prediction horizon is constructed. Following, the current reference is aggregated into the output reference vector $\boldsymbol{Y}_{\mathrm{ref}} = [\boldsymbol{y}_{\mathrm{ref}}^T(t_{1,\mathrm{ref}})\ \ \boldsymbol{y}_{\mathrm{ref}}^T(t_{2,\mathrm{ref}})\ \ \ldots\ \ \boldsymbol{y}_{\mathrm{ref}}^T(t_{z,\mathrm{ref}})]^T$. In a next step, according to (14), z unique output vector gradients are computed within the subintervals of the prediction horizon using the nominal OPP switching instants and the corresponding predicted output variables. This yields the gradient matrix $\boldsymbol{M}$. Finally, the modified switching instants $\boldsymbol{t}^* = [t_1^*\ \ t_2^*\ \ \ldots\ \ t_z^*]^T$ are computed by solving the optimization problem

$$\begin{aligned} \underset{\boldsymbol{t}\in\mathbb{R}^z}{\text{minimize}} \quad & \|\boldsymbol{r} - \boldsymbol{M}\boldsymbol{t}\|_{\boldsymbol{Q}}^2 + \lambda_t \|\Delta \boldsymbol{t}\|_2^2 \\ \text{subject to} \quad & kT_s < t_1 < \ldots < t_z < kT_s + T_p\,. \end{aligned} \tag{16}$$

As per the receding horizon policy, the switch positions that fall within the first sampling interval T_s are implemented at the corresponding time instants $\boldsymbol{t}^*$.[7]

[7]For more details on the operation of the control algorithm, the reader is referred to [11].

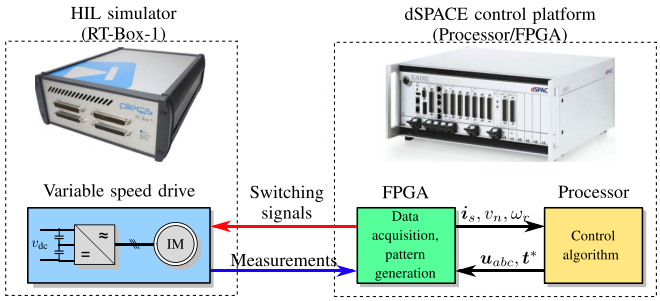

Fig. 6. Block diagram of the hardware-in-the-loop (HIL) test setup.

For a better understanding, the following example is provided.

Example 1: *Consider the drive system in Fig. 1. As depicted in Fig. 5,* $\boldsymbol{u}_{abc}(t_0^-) = [1\,0\,-1]^T$, *with* $t_0 \equiv kT_s$, *is the three-phase switch position applied at the end of the previous sampling interval. According to the illustrated OPP, four nominal switching time instants* $t_{1,\text{ref}}, t_{2,\text{ref}}, t_{3,\text{ref}}$, *and* $t_{4,\text{ref}}$, *with switch positions* $\boldsymbol{u}_{abc}(t_{1,\text{ref}})$, $\boldsymbol{u}_{abc}(t_{2,\text{ref}})$, $\boldsymbol{u}_{abc}(t_{3,\text{ref}})$, *and* $\boldsymbol{u}_{abc}(t_{4,\text{ref}})$, *respectively, fall within the prediction horizon* T_p. *These instants divide the horizon into five subintervals. Within each subinterval, it is assumed that the system output evolves with a constant gradient. Therefore, with the help of the discrete-time model (10) the evolution of the output can be predicted based on the corresponding gradients* $\boldsymbol{m}(t_{\ell,\text{ref}})$. *For example, evolution of one of the controlled variables, i.e.,* $i_{s\alpha}$ *(dash-dotted, magenta line), is shown in Fig. 5 along with its sampled reference (dashed, black line). With the knowledge of the evolution of the system output within the horizon* T_p, *the GP*^{3}*C algorithm manipulates the OPP such that the error between the output and its reference is minimized, e.g., the error between* $i_{s\alpha}$ *and* $i_{s,\text{ref},\alpha}$ *in Fig. 5. In doing so, the modified switching instants* t_1–t_4 *are obtained that result in the stator current shown as solid (green) line. Finally, the (modified) pattern that falls within the first sampling interval* T_s*—shown in red in Fig. 5—is applied to the inverter and the horizon is shifted by one* T_s.

IV. Performance Evaluation of GP^{3}C

This section assesses the effectiveness of the proposed GP^{3}C scheme by means of real-time simulations based on a HIL setup. The block diagram of the HIL system is shown in Fig. 6. It consists of the PLECS RT-Box 1 real-time system which utilizes a Xilinx Z-7030 system-on-chip (SoC). The MV VSD system, shown in Fig. 1, is simulated on the processor of the PLECS RT-Box at a sampling interval of $T_{s,\text{HIL}} = 5\ \mu$s, while the field-programmable gate array (FPGA) is used for the data acquisition (DAQ). The measurements acquired from the VSD system are fed to the dSPACE control platform via an analog interface, while the switching signals for the three-level NPC inverter are received via digital inputs. For more details on the HIL setup, the reader is referred to [26].

The proposed control algorithm is implemented on the dSPACE SCALEXIO system which is based on a 2.8 GHz Intel i7 processor and a Xilinx Kintex-7 FPGA. The controller is implemented on the processor, and the data acquisition and the generation of the switching signals is done on the FPGA. The sampling interval is $T_s = 50\,\mu$s and a 16-step prediction horizon (i.e., $N_p = 16$) is chosen. The various parameters of the drive system are provided in Table I. Note that for the given parameters, a total leakage reactance $X_\sigma = 0.255\,p.u.$ results. The dc-link voltage of the inverter is assumed to be constant. The weighting factors appearing in the objective function (15) are chosen as $\lambda_t = 1 \cdot 10^6$ and $\lambda_n = 5$. The OPP in use has pulse number $d = 5$, while the modulation index is $m = 1.046$, unless otherwise stated. Finally, all results are shown in the p.u. system.

A. Steady-State Operation

To assess the steady-state behavior of the MV drive system, operation at nominal speed and rated torque is considered. This means that the desired electromagnetic torque is $T_e = 1\,p.u.$, while the device switching frequency is 250 Hz since the chosen OPP has $d = 5$, and $f_1 = 50$ Hz. The corresponding results are presented in Fig. 7.[8] Starting with Fig. 7(a), which depicts the three-phase stator current over one fundamental period, it can be seen that the current reference tracking capability of the controller is excellent. Specifically, the deviations of the produced current from its optimal reference trajectory are only minute. As a result, the harmonic energy is very low, as indicated by the current TDD I_{TDD} of 4.274%, which is very close to its theoretically minimum value. Furthermore, the harmonic energy is concentrated at frequencies that are odd, non-triplen integer multiples of the fundamental. This is thanks to the symmetry properties of the nominal OPP, which are preserved—to some extent—by the controller, as can be in Fig. 7(c) where the three-phase switching pattern generated by the controller is shown. As a result of the excellent tracking of the current reference trajectory, accurate tracking of the electromagnetic torque reference is also achieved, see Fig. 7(d). Finally, Fig. 7(e), shows that the controller successfully balances the NP potential around its reference. This is not realized at the expense of the current reference tracking performance, thus clearly demonstrating the multiple-input multiple-output (MIMO) feature and high versatility of the proposed control scheme.

Furthermore, for bench-marking purposes, the performance of the proposed GP^{3}C scheme is compared with that of two established control strategies, namely, finite control set MPC (FCS-MPC) [27] and field oriented control (FOC) with space vector modulation (SVM) [10]. This is done over the range of switching frequencies that are relevant for MV drives, specifically within the range of $f_{\text{sw}} \in [100, 500]$ Hz. For the presented analysis, and in line with the previous tests, operation at nominal speed and rated torque is considered. The associated trade-off curves between current TDD I_{TDD} and switching frequency f_{sw} are shown in Fig. 8. As evident from the results, the proposed control approach achieves significantly lower current TDD values than the other two control methods against which it is benchmarked. This reduction in harmonic current distortions becomes especially pronounced as the switching frequency decreases, where I_{TDD} decreases by at least a factor of two. Thus, Fig. 8

[8] The HIL measurements are recorded by a digital oscilloscope with a sampling frequency of 20 kHz.

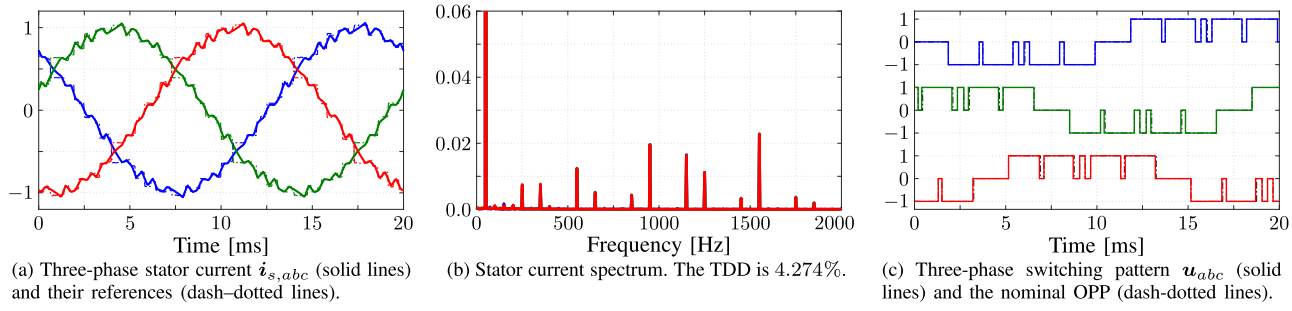

(a) Three-phase stator current $\boldsymbol{i}_{s,abc}$ (solid lines) and their references (dash–dotted lines).
(b) Stator current spectrum. The TDD is 4.274%.
(c) Three-phase switching pattern $\boldsymbol{u}_{abc}$ (solid lines) and the nominal OPP (dash-dotted lines).
(d) Electromagnetic torque T_e (solid line) and its reference (dash–dotted line).
(e) Neutral point potential v_n.
(f) Neutral point current i_n.

Fig. 7. HIL results of the proposed GP^{3}C algorithm at steady-state operation, nominal speed and rated torque. The modulation index is $m = 1.046$, the pulse number $d = 5$, and the switching frequency is 250 Hz.

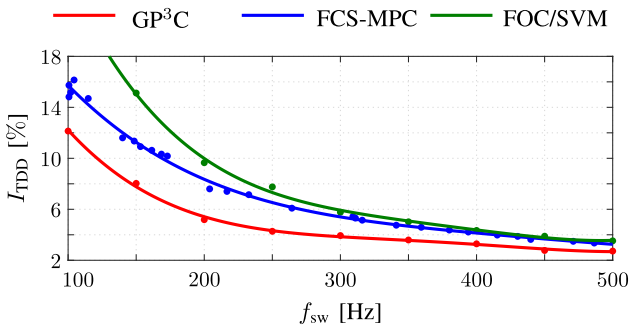

Fig. 8. Trade-off between current TDD I_{TDD} and switching frequency f_{sw} for the proposed GP^{3}C scheme, one-step FCS-MPC and FOC with SVM.

clearly showcases the superior performance of the proposed GP^{3}C during steady-state operating conditions as well as its suitability for operation at low switching frequencies.

B. Operation During Transients

To verify the effectiveness of the proposed GP^{3}C scheme during transient operating conditions, its performance is tested for step changes in the desired torque. While operating at nominal speed, the torque reference is stepped down from $T_{e,\text{ref}} = 1$ to 0 p.u. at $t = 20$ ms, see Fig. 9. Moreover, for reasons of completeness, a second case is examined where the torque reference is returned to its nominal value at $t = 20$ ms from no-load operating conditions, see Fig. 10. As observed in both of the aforementioned figures, the stator currents precisely follow their new reference values, leading to an excellent tracking of the torque reference, see Figs. 9(c) and 10(c). Despite the big changes in the torque reference, GP^{3}C manages to quickly settle to the new operating points by significantly modifying the nominal OPP accordingly. This is clearly shown in Fig. 11, which zooms in on the time axis between $t = 19$ ms and 25 ms to show the control actions in detail. Additionally, the torque does not exhibit any overshoots during the step changes, while the settling times for the step-down and step-up tests are 3 ms and 4.7 ms, respectively. The former settling time indicates that high-bandwidth ability of the control scheme in discussion. The time required for the step-up transient, however, is somewhat longer due to physical limitations, i.e., the small voltage margin that is available in this scenario.

Notwithstanding the foregoing, the proposed controller modifies the nominal OPP during the torque reference step-up change such that the load angle changes as quickly as possible. For example, as can be seen in Fig. 11(e), this is done by significantly reducing the width of the pulses in all the phases and effectively removing the switching pulses in phases a and c. These results clearly show that the dynamic performance of GP^{3}C is excellent and it is only limited by the available dc-link voltage.

Finally, Figs. 9(d) and 10(d) show that the NP potential is kept balanced around zero, despite the large changes in the torque as well as operation at zero torque. With regards to the latter, as mentioned, balancing the NP potential at zero torque is challenging because the vectors (in the $\alpha\beta$-frame) of the applied voltage and stator current are perpendicular. Hence, this figure demonstrates the effectiveness of the active balancing mechanism of the proposed control method even when operating under such challenging conditions, i.e., zero power factor.

C. Operation Across a Discontinuity in the Switching Angles

As shown in Fig. 3(a), the switching angles of the OPP exhibit multiple discontinuities. When operating at a modulation index in the vicinity of such discontinuities, small fluctuations in the dc-link voltage or speed, or big changes in the torque can lead to frequent changes in the modulation index. This, in turn, results

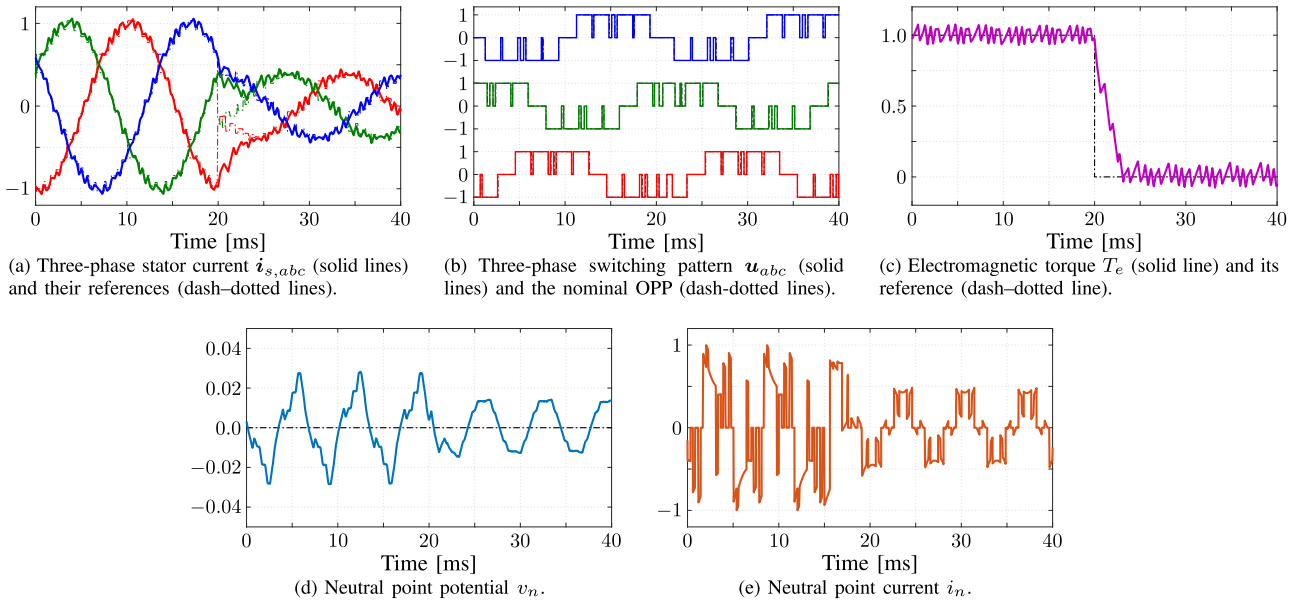

(a) Three-phase stator current $\boldsymbol{i}_{s,abc}$ (solid lines) and their references (dash–dotted lines).

(b) Three-phase switching pattern $\boldsymbol{u}_{abc}$ (solid lines) and the nominal OPP (dash-dotted lines).

(c) Electromagnetic torque T_e (solid line) and its reference (dash–dotted line).

(d) Neutral point potential v_n.

(e) Neutral point current i_n.

Fig. 9. HIL results during a torque reference step-down change (rated load to no load) when operating at nominal speed.

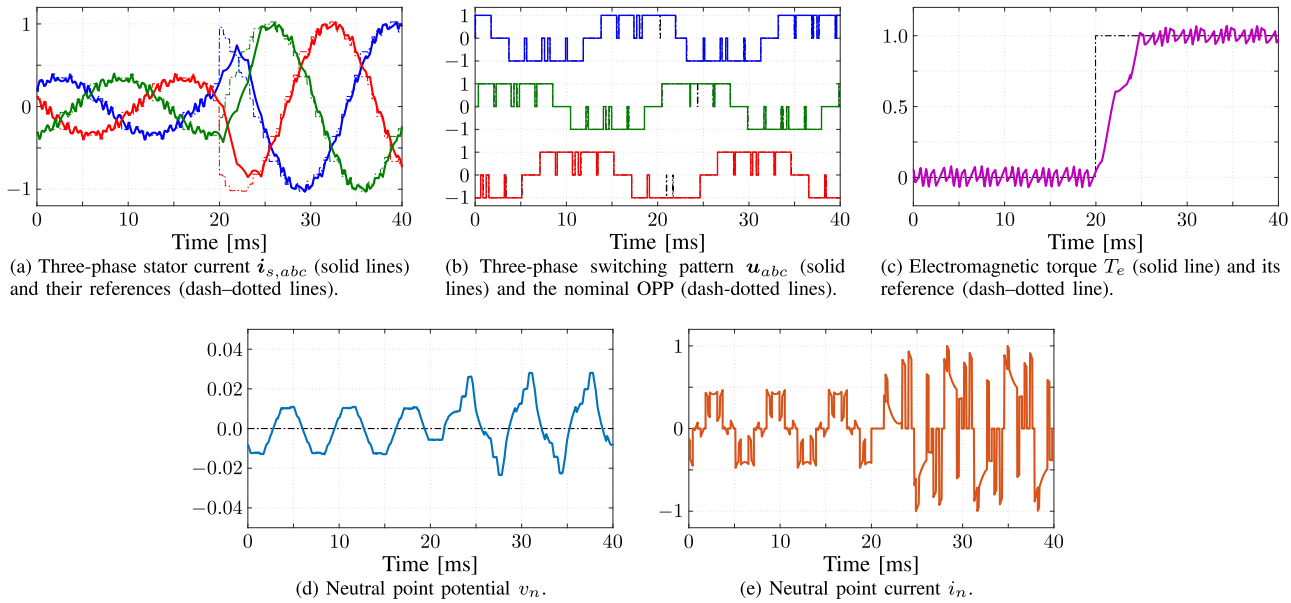

(a) Three-phase stator current $\boldsymbol{i}_{s,abc}$ (solid lines) and their references (dash–dotted lines).

(b) Three-phase switching pattern $\boldsymbol{u}_{abc}$ (solid lines) and the nominal OPP (dash-dotted lines).

(c) Electromagnetic torque T_e (solid line) and its reference (dash–dotted line).

(d) Neutral point potential v_n.

(e) Neutral point current i_n.

Fig. 10. HIL results during a torque reference step-up change (no load to rated load) when operating at nominal speed.

in repeated jumps across the discontinuity, and thus significant changes in the pulse pattern. Such a phenomenon can have an adverse effect on the operation of the drive system as current and torque excursions may occur, while additional switching transitions may appear that could potentially lead to an over-frequency trip. Hence, operation close to these discontinuities is challenging, and tends to be a forbidding task for conventional control methods.

To validate the operation of the proposed control scheme around a discontinuity in the switching angles, its performance is tested under step changes in the desired torque.[9] Specifically, the machine is initially operated at rated torque and 82% speed, which corresponds to modulation index $m = 0.8677$. This operating point appears to the right-side of a discontinuity in the switching angles, i.e., the OPP in use is $\boldsymbol{p}(5, 0.8677) = [16.876^\circ \;\; 49.319^\circ \;\; 56.277^\circ \;\; 77.529^\circ \;\; 87.820^\circ]^T$, see Fig. 3(a).

[9]Small fluctuations in the dc-link voltage and/or speed are typically low-pass-filtered to ensure that the modulation index is immune to them, and it thus remains constant.

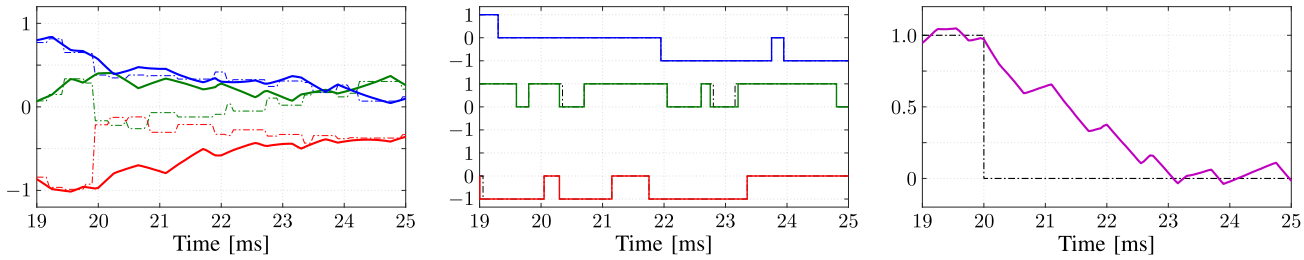

(a) Three-phase stator current $\boldsymbol{i}_{s,abc}$ (solid lines) and their references (dash–dotted lines).
(b) Three-phase switching pattern $\boldsymbol{u}_{abc}$ (solid lines) and the nominal OPP (dash-dotted lines).
(c) Electromagnetic torque T_e.

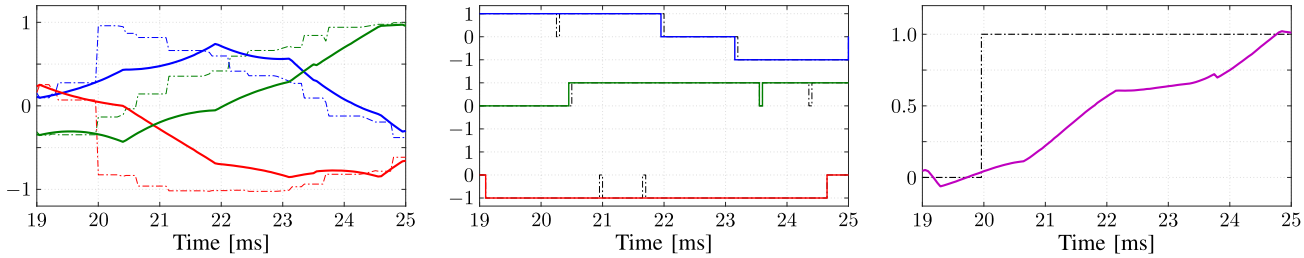

(d) Three-phase stator current $\boldsymbol{i}_{s,abc}$ (solid lines) and their references (dash–dotted lines).
(e) Three-phase switching pattern $\boldsymbol{u}_{abc}$ (solid lines) and the nominal OPP (dash-dotted lines).
(f) Electromagnetic torque T_e.

Fig. 11. Transient performance of GP^{3}C at nominal speed during a torque reference (a)–(c) step-down change, and (d)–(f) step-up change (zoomed in). In (b) and (e), the (black) dash-dotted lines indicate the switching sequence of the unmodified, nominal OPP, whereas the solid lines refer to the modified switching sequence as computed by GP^{3}C.

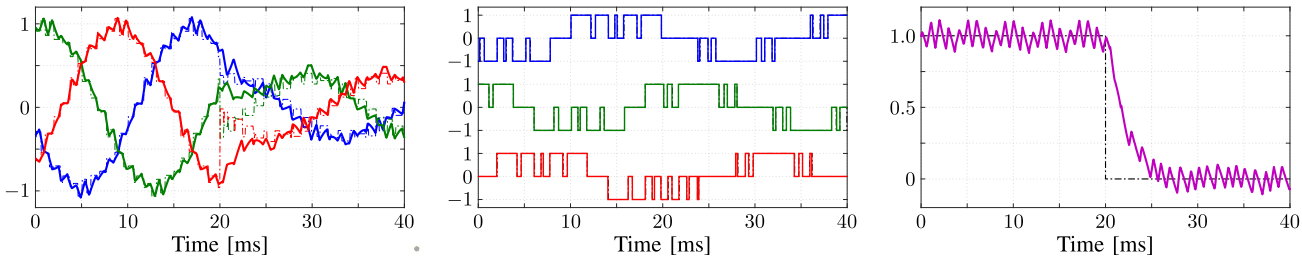

(a) Three-phase stator current $\boldsymbol{i}_{s,abc}$ (solid lines) and their references (dash–dotted lines).
(b) Three-phase switching pattern $\boldsymbol{u}_{abc}$ (solid lines) and the nominal OPP (dash-dotted lines).
(c) Electromagnetic torque T_e (solid line) and its reference (dash–dotted line).

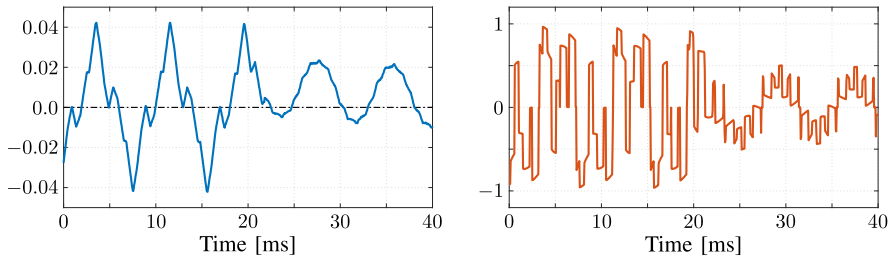

(d) Neutral point potential v_n.
(e) Neutral point current i_n.

Fig. 12. HIL results during a torque reference step-down change (rated load to no load) when operating at 82% speed.

While keeping the rotor speed fixed, the torque reference is stepped down to $T_{e,\text{ref}} = 0$ p.u. at $t = 20$ ms, resulting in the modulation index $m = 0.8584$. This operating point corresponds to the angles on the left-side of the discontinuity, i.e., the new OPP is $\boldsymbol{p}(5, 0.8584) = [28.334^\circ\ 33.187^\circ\ 44.015^\circ\ 50.186^\circ\ 56.741^\circ]^T$. Moreover, the inverse scenario is examined where the torque reference is stepped up from $T_{e,\text{ref}} = 0$ to 1 p.u. The performance of the proposed GP^{3}C scheme across the discontinuity is depicted in Figs. 12 and 13 for the step-down an step-up cases, respectively. Moreover, Fig. 14 zooms in on the time axis to provide a more detailed view on the behavior of the controller during both examined scenarios. As can be observed, the controller operates smoothly across the discontinuity in the switching angles as

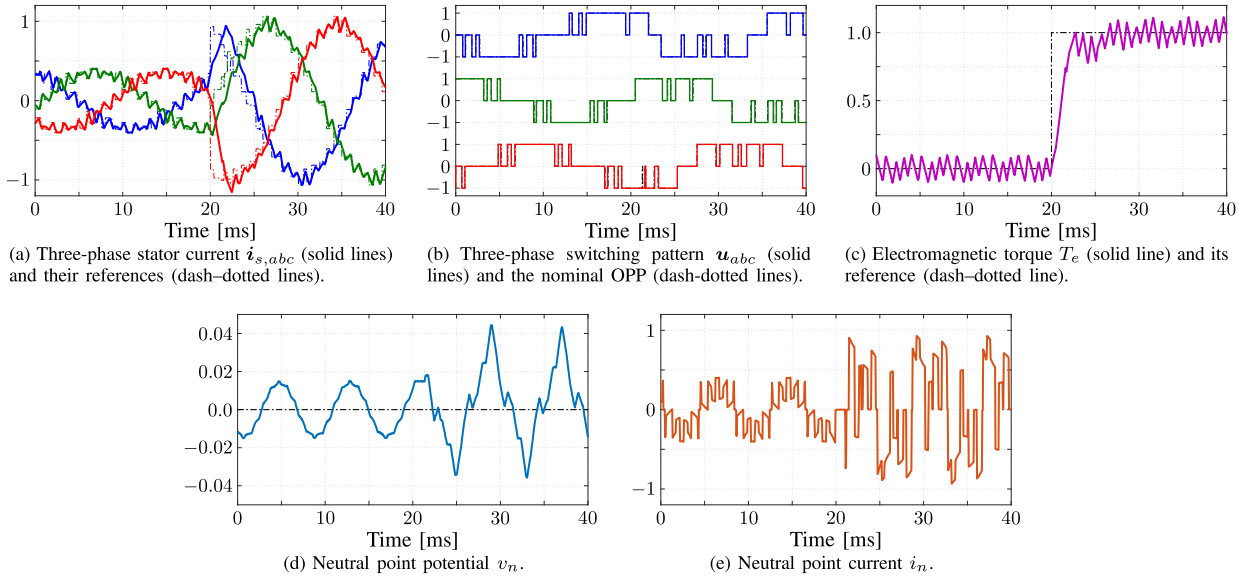

(a) Three-phase stator current $\boldsymbol{i}_{s,abc}$ (solid lines) and their references (dash–dotted lines).
(b) Three-phase switching pattern $\boldsymbol{u}_{abc}$ (solid lines) and the nominal OPP (dash-dotted lines).
(c) Electromagnetic torque T_e (solid line) and its reference (dash–dotted line).
(d) Neutral point potential v_n.
(e) Neutral point current i_n.

Fig. 13. HIL results during a torque reference step-up change (no load to rated load) when operating at 82% speed.

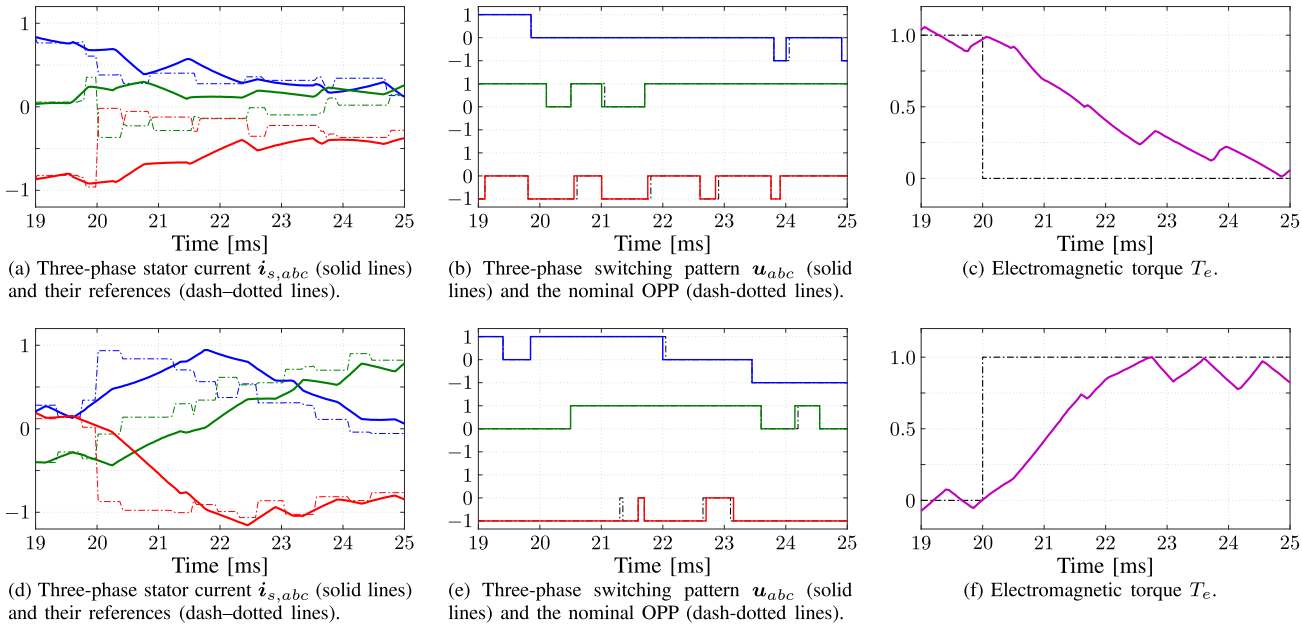

(a) Three-phase stator current $\boldsymbol{i}_{s,abc}$ (solid lines) and their references (dash–dotted lines).
(b) Three-phase switching pattern $\boldsymbol{u}_{abc}$ (solid lines) and the nominal OPP (dash-dotted lines).
(c) Electromagnetic torque T_e.
(d) Three-phase stator current $\boldsymbol{i}_{s,abc}$ (solid lines) and their references (dash–dotted lines).
(e) Three-phase switching pattern $\boldsymbol{u}_{abc}$ (solid lines) and the nominal OPP (dash-dotted lines).
(f) Electromagnetic torque T_e.

Fig. 14. Transient performance of GP^{3}C at 82% speed during a torque reference (a)–(c) step-down change, and (d)–(f) step-up change (zoomed in).

it changes seamlessly between the different OPPs. This is achieved while exhibiting favorable dynamic performance without excursions in the torque and/or stator current, thus ensuring the continuous and safe operation of the drive.

D. Evaluation of the Active NP Potential Balancing Mechanism

To further investigate the NP potential balancing ability of the proposed algorithm, the drive system is tested under two different torque scenarios, i.e., under rated torque and under zero torque[10] conditions. As mentioned earlier, the latter operating point is acknowledged as a critical one for three-level NPC converters [15].

Starting with the first scenario, operation of the drive at nominal speed and rated torque is considered. The initial value of the NP potential is offset by 0.1 p.u.. The weighting factor λ_n is varied and the resulting performance is shown in Fig. 15. As can

[10]This case pertains to a scenario with no mechanical load, where only magnetizing current flows through the stator winding. This implies that the phase difference between the converter voltage and current approaches 90°.

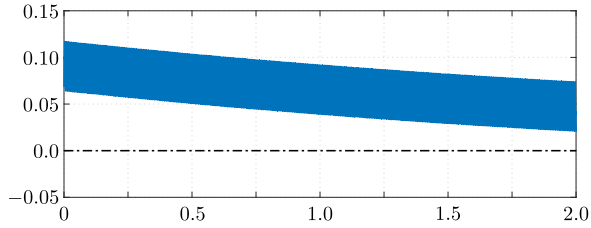

(a) Open-loop natural balancing at rated torque.

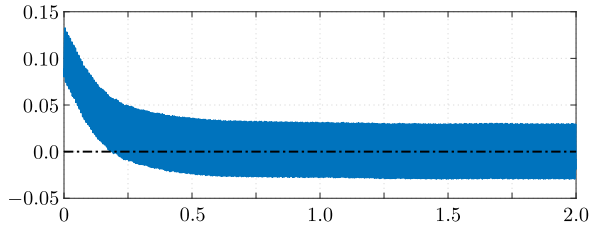

(b) $\lambda_n = 0$.

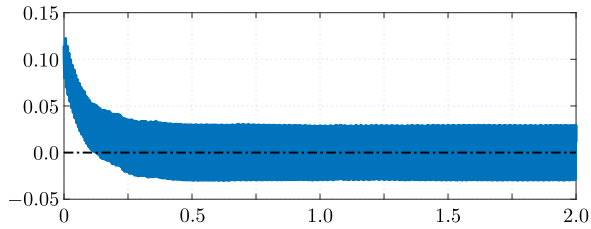

(c) $\lambda_n = 5$.

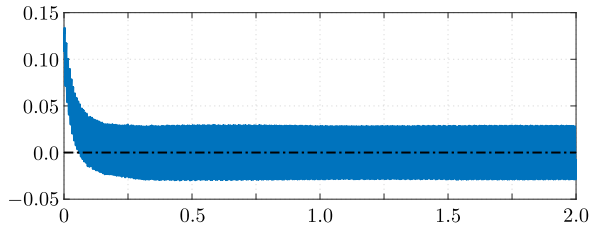

(d) $\lambda_n = 25$.

Fig. 15. Comparison of natural balancing and NP potential balancing for different values of λ_n when operating at rated torque. The initial offset of the NP potential is 0.1 p.u.

be inferred, the closed-loop natural balancing of the NP potential, i.e., when $\lambda_n = 0$ (see Fig. 15(b)), is slower compared with the active NP balancing achieved with the proposed controller, i.e., when $\lambda_n > 0$. Specifically, as the controller prioritizes the NP potential balancing, i.e., as λ_n increases, the NP potential is balanced faster, see Fig. 15(c) and (d). It is also worth noting that the closed-loop natural balancing of GP^{3}C is significantly faster than the open-loop natural balancing of the nominal OPPs, see Fig. 15(b) and (a), respectively.

As for the second test, this is performed at nominal speed and zero torque. An initial offset of 0.1 p.u. is again introduced to the NP potential. The open-loop response of the NP potential (see Fig. 16(a)) has an average decay rate of 0.018 p.u. per second and thus it takes around 15 s to remove the offset. On the contrary, the proposed GP^{3}C scheme balances the NP potential almost thirty times faster, as it drives it to zero within around 0.5 s, see

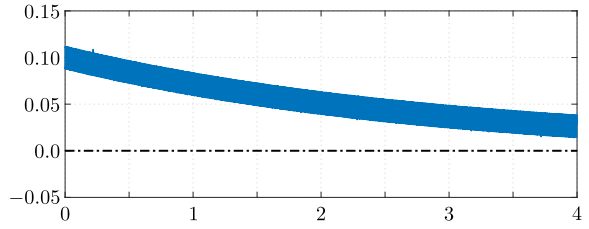

(a) Open-loop natural balancing at zero torque.

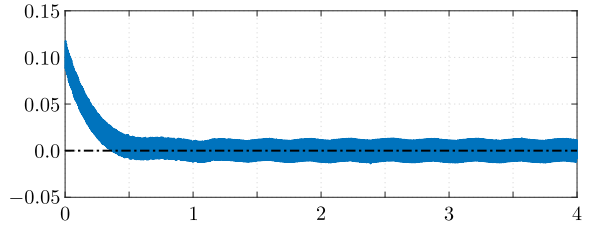

(b) Active NP potential balancing with $\lambda_n = 5$.

Fig. 16. Comparison of natural balancing and NP potential balancing when operating at zero torque. The initial offset of the NP potential is 0.1 p.u.

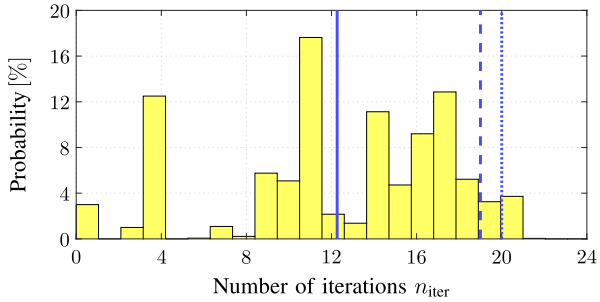

Fig. 17. Probability distribution of the number of iteration steps required by the QP solver to find a solution. The average number of iterations is indicated by the solid vertical line. The 95 and 99 percentiles are shown as dashed and dotted vertical lines, respectively.

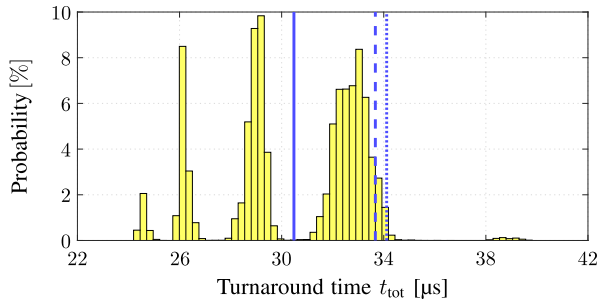

Fig. 18. Probability distribution of the total turnaround time t_{tot}. The average turnaround time is indicated by the solid vertical line. The 95 and 99 percentiles are shown as dashed and dotted vertical lines, respectively.

Fig. 16(b). These results clearly highlight the inherent ability of the proposed control method to actively and effectively balance the NP potential.

E. Computational Burden

The main obstacle in implementing GP^{3}C in real time is the need to solve the computationally intensive QP problem (16).

To address this, the solver developed in [28] is employed. This solver is tailored to the structure of the optimization problem underlying GP^{3}C as it fully exploits its geometry. Thus, thanks to this highly computationally efficient solver, the computation time involved remains modest. To provide a quantitative measure of this efficiency, Fig. 17 illustrates the probability distribution of the number of iterations n_{iter} the QP solver needs to find the solution. As depicted, an average of 12 iterations is sufficient to achieve this. To further elucidate this point, Fig. 18 illustrates the probability distribution of the total turnaround time t_{tot} for the complete GP^{3}C scheme. As can be seen, in over 95% of instances, the total turnaround time t_{tot} is under 33 μs for the selected controller settings. This highlights the capability of solving the entire GP^{3}C algorithm within the chosen controller sampling interval T_s. This is also reflected by the total maximum turnaround time $t_{tot,\max} = 39.786\,\mu$s, which is smaller than the sampling interval $T_s = 50\,\mu$s, i.e., only about 80% of the available time is used to execute the controller.

V. Conclusion

This paper refined the GP^{3}C algorithm introduced in [11] to incorporate the balancing of the NP potential of a three-level NPC inverter into the control problem. The mathematical model adopted within the framework of the proposed controller equips GP^{3}C with high versatility and enables it to simultaneously address multiple control objectives. To exploit these favorable characteristics, the discussed method was applied to an MV drive system, and its performance was assessed in a real-time environment by employing a HIL system. As highlighted by the presented results, thanks to the combination of optimal constrained control and optimal modulation, the proposed strategy not only exhibits superior performance during steady state, i.e., minimal current TDD for a given switching frequency, but it is characterized by high bandwidth as demonstrated by the short settling times during transients and its ability to quickly balance the NP potential over the whole operating regime. Finally, the presented comparisons with established control methods, such as FOC with SVM and FCS-MPC, further showcased the superior performance of the proposed control method.

Appendix A
System Matrices

The matrices of the continuous-time state-space model in (9) are

$$\boldsymbol{F}(t) = \begin{bmatrix} \boldsymbol{F}_{\text{IM}} & \begin{bmatrix} -\frac{X_r}{D}\boldsymbol{K}\,|\boldsymbol{u}_{abc}(t)| \\ \boldsymbol{0}_{2\times 1} \end{bmatrix} \\ \begin{bmatrix} \frac{1}{2X_{\text{dc}}}\,|\boldsymbol{u}_{abc}(t)|^T\,\boldsymbol{K}^{-1} & \boldsymbol{0}_{1\times 2} \end{bmatrix} & 0 \end{bmatrix},$$

$$\boldsymbol{G} = \frac{v_{\text{dc}}}{2}\frac{X_r}{D}\begin{bmatrix} 1 & 0 \\ 0 & 1 \\ 0 & 0 \\ 0 & 0 \\ 0 & 0 \end{bmatrix}\boldsymbol{K}, \quad \boldsymbol{C} = \begin{bmatrix} 1 & 0 & 0 & 0 & 0 \\ 0 & 1 & 0 & 0 & 0 \\ 0 & 0 & 0 & 0 & 1 \end{bmatrix},$$

where

$$\boldsymbol{F}_{\text{IM}} = \begin{bmatrix} -\frac{1}{\tau_s} & 0 & \frac{X_m}{\tau_r D} & \omega_r\frac{X_m}{D} \\ 0 & -\frac{1}{\tau_s} & -\omega_r\frac{X_m}{D} & \frac{X_m}{\tau_r D} \\ \frac{X_m}{\tau_r} & 0 & -\frac{1}{\tau_r} & -\omega_r \\ 0 & \frac{X_m}{\tau_r} & \omega_r & -\frac{1}{\tau_r} \end{bmatrix}.$$

Appendix B
Objective Function Matrices

The vector $\boldsymbol{r}$ and matrix $\boldsymbol{M}$ in (15) are

$$\boldsymbol{r} = \begin{bmatrix} \boldsymbol{y}_{\text{ref}}(t_{1,\text{ref}}) - \boldsymbol{y}(t_0) \\ \boldsymbol{y}_{\text{ref}}(t_{2,\text{ref}}) - \boldsymbol{y}(t_0) \\ \vdots \\ \boldsymbol{y}_{\text{ref}}(t_{z,\text{ref}}) - \boldsymbol{y}(t_0) \end{bmatrix}$$

and

$$\boldsymbol{M} = \begin{bmatrix} \boldsymbol{m}_{t_0} & \boldsymbol{0}_2 & \dots & \boldsymbol{0}_2 & \boldsymbol{0}_2 \\ \boldsymbol{m}_0 & \boldsymbol{m}_{t_1} & \dots & \boldsymbol{0}_2 & \boldsymbol{0}_2 \\ \vdots & \vdots & \ddots & \vdots & \vdots \\ \boldsymbol{m}_0 & \boldsymbol{m}_1 & \dots & \boldsymbol{m}_{t_{z-2}} & \boldsymbol{0}_2 \\ \boldsymbol{m}_0 & \boldsymbol{m}_1 & \dots & \boldsymbol{m}_{z-2} & \boldsymbol{m}_{t_{z-1}} \end{bmatrix}$$

with

$$\boldsymbol{m}_{t_\ell} = \boldsymbol{m}(t_{\ell,\text{ref}})$$
$$\boldsymbol{m}_\ell = \boldsymbol{m}(t_{\ell,\text{ref}}) - \boldsymbol{m}(t_{\ell+1,\text{ref}})$$

where $\ell \in \{0, 1, 2, \dots, z-1\}$.

References

[1] A. K. Rathore, J. Holtz, and T. Boller, "Synchronous optimal pulsewidth modulation for low-switching-frequency control of medium-voltage multilevel inverters," *IEEE Trans. Ind. Electron.*, vol. 57, no. 7, pp. 2374–2381, Jul. 2010.

[2] J. Rodriguez and P. Cortes, *Predictive Control of Power Converters and Electrical Drives*. Hoboken, NJ, USA: Wiley, 2012.

[3] G. S. Buja and G. B. Indri, "Optimal pulsewidth modulation for feeding AC motors," *IEEE Trans. Ind. Appl.*, vol. IA-13, no. 1, pp. 38–44, Jan. 1977.

[4] G. S. Buja, "Optimum output waveforms in PWM inverters," *IEEE Trans. Ind. Appl.*, vol. IA-16, no. 6, pp. 830–836, Nov. 1980.

[5] J. Holtz and N. Oikonomou, "Synchronous optimal pulsewidth modulation and stator flux trajectory control for medium-voltage drives," *IEEE Trans. Ind. Appl.*, vol. 43, no. 2, pp. 600–608, Mar./Apr. 2007.

[6] J. Holtz and B. Beyer, "Optimal synchronous pulsewidth modulation with a trajectory-tracking scheme for high-dynamic performance," *IEEE Trans. Ind. Appl.*, vol. 29, no. 6, pp. 1098–1105, Nov./Dec. 1993.

[7] J. Holtz and B. Beyer, "The trajectory tracking approach-A new method for minimum distortion PWM in dynamic high-power drives," *IEEE Trans. Ind. Appl.*, vol. 30, no. 4, pp. 1048–1057, Jul./Aug. 1994.

[8] T. Geyer, N. Oikonomou, G. Papafotiou, and F. D. Kieferndorf, "Model predictive pulse pattern control," *IEEE Trans. Ind. Appl.*, vol. 48, no. 2, pp. 663–676, Mar./Apr. 2012.

[9] N. Oikonomou, C. Gutscher, P. Karamanakos, F. D. Kieferndorf, and T. Geyer, "Model predictive pulse pattern control for the five-level active neutral-point-clamped inverter," *IEEE Trans. Ind. Appl.*, vol. 49, no. 6, pp. 2583–2592, Nov./Dec. 2013.

[10] T. Geyer, V. Spudić, W. van der Merwe, and E. Guidi, "Model predictive pulse pattern control of medium-voltage neutral-point-clamped inverter drives," in *Proc. IEEE Energy Convers. Congr. Expo.*, 2018, pp. 5047–5054.

[11] M. A. W. Begh, P. Karamanakos, and T. Geyer, "Gradient-based predictive pulse pattern control of medium-voltage drives–Part I: Control, concept and analysis," *IEEE Trans. Power Electron.*, vol. 37, no. 12, pp. 14222–14236, Dec. 2022.

[12] H. du Toit Mouton, "Natural balancing of three-level neutral-point-clamped PWM inverters," *IEEE Trans. Ind. Electron.*, vol. 49, no. 5, pp. 1017–1025, Oct. 2002.
[13] J. K. Steinke, "Switching frequency optimal PWM control of a three-level inverter," *IEEE Trans. Power Electron.*, vol. 7, no. 3, pp. 487–496, Jul. 1992.
[14] S. Ogasawara and H. Akagi, "Analysis of variation of neutral point potential in neutral-point-clamped voltage source PWM inverters," in *Proc. IEEE Conf. Rec. Ind. Appl. 28th IAS Annu. Meeting*, 1993, pp. 965–970.
[15] C. Newton and M. Sumner, "Neutral point control for multi-level inverters: Theory, design and operational limitations," in *Proc. IEEE Ind. App. Soc. Annu. Mtg.*, 1997, pp. 1336–1343.
[16] J. Pou, R. Pindado, D. Boroyevich, and P. Rodríguez, "Evaluation of the low-frequency neutral-point voltage oscillations in the three-level inverter," *IEEE Trans. Ind. Electron.*, vol. 52, no. 6, pp. 1582–1588, Dec. 2005.
[17] J. Holtz and N. Oikonomou, "Neutral point potential balancing algorithm at low modulation index for three-level inverter medium-voltage drives," *IEEE Trans. Ind. Appl.*, vol. 43, no. 3, pp. 761–768, May/Jun. 2007.
[18] T. Boller, J. Holtz, and A. K. Rathore, "Neutral-point potential balancing using synchronous optimal pulsewidth modulation of multilevel inverters in medium-voltage high-power AC drives," *IEEE Trans. Ind. Appl.*, vol. 50, no. 1, pp. 549–557, Jan./Feb. 2014.
[19] T. Geyer and V. Spudić, "Model predictive pulse pattern control with integrated balancing of the neutral point potential," in *Proc. IEEE 21st Eur. Conf. Power Electron. Appl.*, 2019, pp. P.1–P.10.
[20] M. A. W. Begh, P. Karamanakos, and T. Geyer, "Gradient-based predictive 569 pulse pattern control with active neutral point balancing for three-level inverter medium-voltage drives," in *Proc. IEEE Energy Convers. Congr. Expo.*, 2022, pp. 1–8.
[21] T. Geyer, *Model Predictive Control of High Power Converters and Industrial Drives*. Hoboken, NJ, USA: Wiley, 2016.
[22] J. Holtz, "The representation of AC machine dynamics by complex signal flow graphs," *IEEE Trans. Ind. Electron.*, vol. 42, no. 3, pp. 263–271, Jun. 1995.
[23] P. Karamanakos, R. Mattila, and T. Geyer, "Fixed switching frequency direct model predictive control based on output current gradients," in *Proc. IEEE 44th Annu. Conf. IEEE Ind. Electron. Soc.*, 2018, pp. 2329–2334.
[24] P. Karamanakos, M. Nahalparvari, and T. Geyer, "Fixed switching frequency direct model predictive control with continuous and discontinuous modulation for grid-tied converters with LCL filters," *IEEE Trans. Control Sys. Technol.*, vol. 29, no. 4, pp. 1503–1518, Jul. 2021.
[25] Q. Yang et al., "A fixed switching frequency direct model predictive control for neutral-point-clamped three-level inverters with induction machines," *IEEE Trans. Power Electron.*, vol. 38, no. 11, pp. 13703–13716, Nov. 2023.
[26] M. A. W. Begh, P. Karamanakos, T. Geyer, and Q. Yang, "Gradient-based predictive pulse pattern control of medium-voltage drives–Part II: Performance assessment," *IEEE Trans. Power Electron.*, vol. 37, no. 12, pp. 14237–14251, Dec. 2022.
[27] A. Tregubov, P. Karamanakos, and L. Ortombina, "Long-horizon robust direct model predictive control for medium-voltage induction motor drives with reduced computational complexity," *IEEE Trans. Ind. Appl.*, vol. 59, no. 2, pp. 1775–1787, Mar./Apr. 2023.
[28] Q. Yang et al., "Computationally efficient fixed switching frequency direct model predictive control," *IEEE Trans. Power Electron.*, vol. 37, no. 3, pp. 2761–2777, Mar. 2022.

Mirza Abdul Waris Begh (Member, IEEE) received the B.Tech. degree in electrical engineering from NIT Hamirpur, Hamirpur, India, in 2014, and the M.Sc. degree in electrical power engineering from Technische Universität München, Munich, Germany, in 2018. Since 2019, he has been working toward the Ph.D. degree in electrical engineering with the Faculty of Information Technology and Communication Sciences, Tampere University, Tampere, Finland.

From 2014 to 2015, he was with the ABB Global R&D Centre, Bangalore, India, where he worked on low-voltage drives and PLCs. From 2015 to 2016, he was a University Lecturer with the Institute of Technology, University of Kashmir, Srinagar, India. In 2018, he was with the Fraunhofer Institute for Solar Energy Systems, where he worked on the design of control methods for grid-connected systems. In 2022, he joined Danfoss Drives, Tampere, Finland, as a Control Engineer. His research interests include electric drives, optimal modulation methods, optimal control, and embedded implementation of control algorithms.

Petros Karamanakos (Senior Member, IEEE) received the Diploma and Ph.D. degree in electrical and computer engineering from the National Technical University of Athens, Athens, Greece, in 2007 and 2013, respectively.

From 2010 to 2011, he was with the ABB Corporate Research Center, Baden-Dättwil, Switzerland, where he worked on model predictive control strategies for medium-voltage drives. From 2013 to 2016, he was a PostDoc Research Associate with the Chair of Electrical Drive Systems and Power Electronics, Technische Universität München, Munich, Germany. Since 2016, he has been with the Faculty of Information Technology and Communication Sciences, Tampere University, Tampere, Finland, where he is currently an Associate Professor. His research interests include the intersection of optimal control, mathematical programming, and power electronics, including model predictive control and optimal modulation for utility-scale power converters and ac variable speed drives.

He was the recipient of the 2014 Third Best Paper Award of the IEEE Transactions on Industry Applications and four Prize Paper Awards at IEEE conferences. He is an Associate Editor for IEEE TRANSACTIONS ON INDUSTRY APPLICATIONS. Since 2022, he has been a Regional Distinguished Lecturer of the IEEE Power Electronics Society.

Tobias Geyer (Fellow, IEEE) received the Dipl.-Ing. degree in electrical engineering, the Ph.D. degree in control engineering, and the Habilitation degree in power electronics from ETH Zurich, Zurich, Switzerland, in 2000, 2005, and 2017, respectively.

He spent three years with the GE Global Research, Munich, Germany, and University of Auckland, Auckland, New Zealand, and eight years with ABB's Corporate Research Centre, Baden-Dättwil, Switzerland. In 2020, he joined ABB's Medium-Voltage Drive division as R&D platform Manager of the ACS6080. In 2022, he became a Corporate Executive Engineer. Since 2017, he has been an extraordinary Professor with Stellenbosch University, Stellenbosch, South Africa.

He is the author of more than 40 patent families, 160 publications, and the book *Model Predictive Control of High-Power Converters and Industrial Drives* (Wiley, 2016). He teaches a regular course on model predictive control with ETH Zurich. His research interests include medium-voltage and low-voltage drives, utility-scale power converters, optimized pulse patterns, and model predictive control.

He was the recipient of the IEEE PELS Modeling and Control Technical Achievement Award in 2022, Semikron Innovation Award in 2021, and Nagamori Award in 2021. He was also the recipient of the two Prize Paper Awards of IEEE Transactions and three Prize Paper Awards at IEEE conferences. He is a former Associate Editor for IEEE TRANSACTIONS ON INDUSTRY APPLICATIONS from 2011 to 2014 and IEEE TRANSACTIONS ON POWER ELECTRONICS from 2013 to 2019. In 2018, he was an International Program Committee Vice Chair of the IFAC conference on Nonlinear Model Predictive Control, Madison, WI, USA. From 2020 to 2023, he was a Distinguished Lecturer of the IEEE Power Electronics Society.